Advances in Geo-Energy Research

Vol. 21, No. 3, p. 283-296, 2026

Original article

In-situ observation and mechanistic investigation of bubble-size effects on gas hydrate formation and dissociation at the pore scale

Leyan Wen[1], Changqi Li[1], Ruilu Zhang[1], Yang Yu[1,2], Yajun Deng[1]*, Hailong Lu[3]

[1]*Future Technology School, Shenzhen Technology University, Shenzhen 518118, P. R. China*

[2]*School of Safety Science, Tsinghua University, Beijing 100084, P. R. China*

[3]*Beijing International Center for Gas Hydrate, School of Earth and Space Sciences, Peking University, Beijing 100871, P. R. China*

Keywords:
Microfluidic chip
natural gas hydrate
gas bubbles
bubble-size regulation
hydrate formation and dissociation

Cited as:
Wen, L., Li, C., Zhang, R., Yu, Y., Deng, Y., Lu, H. *In-situ* observation and mechanistic investigation of bubble-size effects on gas hydrate formation and dissociation at the pore scale. Advances in Geo-Energy Research, 2026, 21(3): 283-296.
https://doi.org/10.46690/ager.2026.09.07

Abstract:
Natural gas hydrates represent a promising clean energy resource, whose multiphase evolution in subsea sediments, especially in association with seafloor gas seepage and bubble formation, remains poorly understood at the pore scale. To address this gap, this study aimed to quantitatively investigate how bubble size modulates the kinetics of hydrate formation and dissociation by employing high-pressure microfluidics under seafloor reservoir-relevant thermodynamic conditions. *In-situ* visualization uncovered a two-stage formation mechanism around gas bubbles: Rapid hydrate shell formation followed by gradual shell densification. The shell formation was found to be governed by local gas concentration gradients and exhibited a "chain induction" effect between adjacent bubbles, while the densification duration scaled linearly with bubble size. Likewise, hydrate dissociation was shown to follow a two-stage pathway: The internal hydrate dissociates rapidly in the initial stage, after which the remaining hydrate dissociates much more slowly because the intact dense outer shell restricts outward gas diffusion and internal pressure buildup weakens the thermodynamic driving force. These findings reveal the bubble-size-regulated pore-scale mechanism, providing a kinetic foundation for the dynamic optimization of natural gas hydrate exploitation.

1. Introduction

Natural gas hydrates are ice-like crystals formed by natural gas and water under high-pressure and low-temperature conditions (Sloan, 2003). They are abundantly distributed in terrestrial permafrost and marine sediments (water depth > 300 m). Direct deep-sea observations have documented gas hydrate mounds and associated chemosynthetic communities at 3,640 m on the Molloy Ridge (Panieri et al., 2025). Global in-place natural gas hydrate resources are estimated at 2×10^{15} m^3, exceeding twice the carbon content of all known fossil fuels combined (Cui et al., 2018; Yin et al., 2018). One cubic meter of methane hydrate releases 164 m^3 of methane under standard conditions (Jang and Santamarina, 2016), offering high energy density and positioning hydrates as a strategic clean energy option for future sustainability (Pang et al., 2024; Zhang et al., 2024b). Over the past two decades, several countries such as the United States, China, Japan, Canada, and India have conducted extensive laboratory studies and field trials on this topic.

Energy recovery from deep-sea gas hydrates is governed by coupled gas-liquid-solid interactions and microscale multiphase flow behaviors in sediments (Fang et al., 2025; Gong

Yandy Scientific Press

*Corresponding author.
E-mail address: heyoukeke@gmail.com (L. Wen); lcq13428528568@163.com (C. Li); amnesiatoma@outlook.com (R. Zhang); yuyang1@mail.tsinghua.edu.cn (Y. Yu); dengyajun@sztu.edu.cn (Y. Deng); hlu@pku.edu.cn (H. Lu).
2207-9963 © The Author(s) 2026.
Received July 25, 2026; revised August 22, 2026; accepted September 10, 2026; available online September 11, 2026.

et al., 2025). Current major production strategies include thermal stimulation, depressurization, inhibitor injection, and CO_2 replacement (Zhang et al., 2019). Thermal stimulation strategies are an effective approach to destabilize hydrate structures and trigger dissociation for methane release. The 2002 Mallik field test has confirmed their feasibility (Moridis et al., 2004; Uddin et al., 2014); however, their commercial application is hindered by prohibitive energy costs and low overall efficiency (Islam, 1994; Tang et al., 2006). To address these limitations, the kinetics of hydrate formation and dissociation must be explained from a gas-liquid-solid triple-phase perspective. Moreover, the thermal stimulation of hydrates typically generates abundant microbubbles that strongly influence the reaction dynamics. Elucidating this mechanism can help enhance energy utilization during exploitation and provide theoretical guidance for optimizing the thermal stimulation of hydrates.

Traditional experimental methods for hydrate are constrained by limited spatial resolution and high costs, making it challenging to observe multiphase interactions at the pore scale. As an alternative, microfluidics has emerged as a pivotal tool in methane hydrate research, enabling high-resolution visualization and precise parametric control (Liu et al., 2023; Lu et al., 2025). Micromodels replicating sedimentary pore networks enable the correlation of pore-scale phenomena with macroscopic behaviors during the process of hydrate exploitation (Zhang et al., 2025a). Similarly, complementary image-based approaches, such as the X-ray computed tomography (CT)-based three-dimensional reconstruction of porous and fractured media, have been used to characterize pore-fracture geometry and its control on fluid flow (Wang et al., 2016, 2021, 2022). Using this combined with microfluidics, recent studies have identified key nucleation pathways, such as heating-induced ice-to-hydrate conversion (Li et al., 2020, 2022) and pressure-pulse-induced destabilization (Xu et al., 2023). Morphologically, the growth mode depends heavily on the gas source: Dissolved gas typically yields transparent, acicular crystals, while free gas forms porous, bubble-encapsulating shells (Li et al., 2024; Zhang et al., 2024a, 2024c, 2026). Depending on the local interfacial interactions, these formations can further develop into massive, vein-like, nodular, film-like, or shell architectures (Yao et al., 2019). From a kinetic perspective, this growth is highly anisotropic along the interfaces and is primarily governed by mass diffusion and Ostwald ripening (Almenningen et al., 2021; Li et al., 2021; Liu et al., 2025; Wang et al., 2025). To better capture these complex phases, recent work has integrated AI-based image analysis, extending these microscale insights to CO_2 hydrates as well (Li et al., 2025; Zhong et al., 2025).

At the pore scale, hydrate formation is strictly governed by local thermodynamic and capillary conditions. Initial water saturation dictates the predominant hydrate habit (Li et al., 2022), whereas higher subcooling accelerates growth and drives a morphological transition from compact to branched structures (Muraoka et al., 2020). These kinetic pathways are further modulated by guest gas composition (Li et al., 2014b). Beyond the initial growth phase, repeated formation-dissociation cycles induce severe pore-scale reorganization, which can degrade reservoir permeability by up to an order of magnitude (Ji et al., 2021; Zhang et al., 2025b). This strong sensitivity of permeability to pore-scale structure has also been observed in other gas-bearing porous media, where fracture connectivity and geometry, in line with dual-porosity transport, govern fluid seepage and gas extraction (Xu et al., 2022, 2024).

Although recent studies have examined the macroscopic kinetics and behaviors of hydrate formation and dissociation, they have focused predominantly on continuous gas-phase systems, and research addressing pore-scale gas migration mechanisms is yet emerging (Sun et al., 2025). Recent microfluidic work has begun to resolve methane migration in oceanic hydrate systems, yet the role of discrete bubble size remains unresolved (Wang et al., 2024). In fact, during thermal stimulation, the phase-transition dynamics of hydrates are critically governed by the dynamic evolution of discrete free gas bubbles. To this end, the quantitative impacts of discrete free gas bubble size on the full formation-dissociation kinetic cycle of natural gas hydrate remain poorly quantified and studied. In particular, the governing mechanisms by which bubble size regulates initial hydrate shell formation, densification duration, and dissociation regime transition remain ambiguous. Hydrate formation on bubble surfaces in South China Sea seepage areas is strongly pressure-gradient dependent (Zhou et al., 2024), but a size-resolved description across the full formation-dissociation cycle is still lacking.

A further complication is that bubble-size effects are rarely assessed over a complete formation-dissociation cycle. Formation controls shell thickness, internal gas inventory, and the spatial distribution of residual gas, whereas dissociation inherits this morphology and is therefore governed by a different transport limitation. Treating the two stages separately may obscure how a single initial size descriptor propagates through the pore network. Neighboring bubbles and pore-throat constrictions can also introduce cooperative effects that are absent in isolated single-bubble experiments. Resolving the coupled behavior therefore requires synchronized measurements of bubble geometry, hydrate area, thermodynamic state, and local morphology at the same location. The present experiments address this need by tracking individually resolved bubbles through shell growth, densification, and thermal dissociation under one pressure-temperature program, which allows the size dependence observed in an early stage to be compared directly with that in later stages while preserving the local pore-scale context.

To address the above knowledge gap, this study investigated the bubble size effect on the formation and dissociation kinetics of gas hydrate. The applied high-pressure microfluidic chip replicates the sediment pore network structure and generates monodisperse methane bubbles (projected area $4 \times 10^5 \sim 6 \times 10^5$ μm^2) under simulated deep-sea conditions. Sodium dodecyl sulfate (SDS) was employed as a simplified model surfactant to simulate certain interfacial effects of biogenic surfactants from hydrocarbon-degrading microbes, while avoiding the inconsistent composition of natural biosurfactants and enhancing system controllability (Liu and Shao, 2007; Zhang et al., 2007; Pardhi et al., 2022). For the first time, this work

establishes a quantitative kinetic framework linking bubble size to the two-stage formation and two-stage dissociation of hydrates, moving beyond traditional continuous-phase models to underpin pore-scale optimization of thermal stimulation for marine hydrate production.

2. Methods

2.1 Experimental apparatus and data analysis

To simulate actual seafloor reservoir conditions and monitor pore-scale hydrate dynamics, a customized high-pressure microfluidic platform was utilized, as shown in Fig. 1. This platform follows the recent trend of combining high-pressure microfluidics with *in situ* diagnostics to resolve hydrate phase transitions and mass transfer in confined spaces (Ouyang et al., 2025). This apparatus integrates six modular units into a single platform. The core component, a microfluidic chip, is housed within a high-pressure vessel capable of withstanding up to 16 MPa, secured by an annular metal clamp and composite metal/rubber fasteners with a confining pressure pump maintaining a prescribed confining pressure. The integrated micro-injection and pressure-control module enables the delivery of an aqueous SDS solution with a pressure precision of ±0.5 MPa under system pressures as high as 40 MPa. The system also features a temperature-control unit, consisting of a circulating water bath and a jacketed holder, that can regulate the chip temperature with accuracy of ±0.1 K to reproduce the thermal regime of deep-sea hydrate-bearing sediments. Furthermore, a real-time data acquisition unit feeds a data-logging workstation providing dynamic tracking of thermodynamic changes, which is equipped with temperature and pressure sensors installed at inlet, outlet and confining lines. A two-stage pressure regulator delivers methane to the chip inlet with an accuracy of ±0.01 MPa. Throughout the experiments, hydrate formation and dissociation were captured using a charge-coupled device camera (3,840 × 2,160 pixels, 30 fps), and thermodynamic data were recorded in real time for analysis.

To reproduce the pore structure of seafloor hydrate-bearing sediments, the microfluidic chip was fabricated from hydrophilic borosilicate glass with a static water contact angle of ~ 50° and throat sizes of 200-700 μm. The pore-network morphology of this chip is illustrated in Fig. S1(a). The experimental materials consist of a natural gas mixture (CH_4:C_2H_6:C_3H_8=90:7:3 mol%, a representative of the hydrocarbon composition of real hydrate samples from the northern South China Sea), SDS, and deionized water.

After recording 4K videos, individual frames were extracted for quantitative image analysis (Fig. S1(b)). First, raw frames were calibrated and converted to 8-bit grayscale in ImageJ to enhance image contrast. Dense hydrate regions and the pore matrix were manually labeled, and an iterative training procedure was employed to establish a robust image segmentation model. Hydrate regions were identified using both reflectance/gray-level contrast and morphological continuity. Pore walls, aqueous regions, gas regions, and hydrate regions were labeled separately according to their optical contrast and morphological characteristics. Ambiguous frames

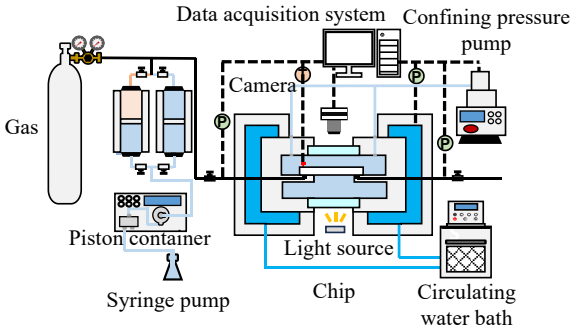


Fig. 1. Schematic of the high-pressure microfluidic system.

were independently reviewed and corrected before quantitative analysis. Subsequently, to check if the output was consistent with the desired threshold results, 10,000+ frames were input into the model in batches according to different generation times. A custom-written ImageJ macro was used to apply this model for batch processing of all images, generating binary masks of hydrate phases. Finally, the projected area, equivalent diameter and number of hydrate particles were quantified for each frame on the basis of these binary masks. For each bubble or hydrate particle, the equivalent circular radius was calculated from the measured projected area as $R_e = \sqrt{A_{proj}/\pi}$, where the first quantity is the equivalent circular radius and the second is the projected area; this radius was used consistently for size classification and statistical analysis. The projected area and equivalent radius were used only as two-dimensional (2D) image-based descriptors.

2.2 Experimental procedure

The hydrate equilibrium pressure for the natural gas mixture at 274 K was calculated to be around 0.94 MPa using the thermodynamic tool developed by Sloan (Ballard et al., 2004). To provide sufficient driving force and promote rapid hydrate formation, experiments were conducted at elevated pressures of 5.8 MPa and a constant temperature of 274 K using a 0.1 wt% SDS solution.

Prior to the experiments, the microfluidic chip was ultrasonically cleaned and thoroughly rinsed with deionized water. After the chip was secured inside the high-pressure vessel, a confining pressure of 1 MPa was applied and maintained at a constant temperature for 1 h. The leak-tight sealing of the system was verified by a pressure variation of less than 0.02 MPa.

To purge air from the microfluidic chip, the SDS solution was injected at a flow rate of 8 mL/min. To prevent fluid leakage, the outlet pressure was set to 7 MPa, and the confining pressure was maintained at 1 MPa higher than the internal pressure to prevent chip damage. The gas mixture was then introduced into the system until the internal pressure reached 5 MPa. Subsequently, gas and liquid were injected alternately to achieve sufficient phase mixing and maximize the gas-liquid interfacial area. Next, the system was cooled to 274 K and these conditions were maintained until hydrate formation was confirmed by *in-situ* optical observation.

The dissociation of gas hydrate was triggered by controlled thermal stimulation. The temperature of the circulating bath

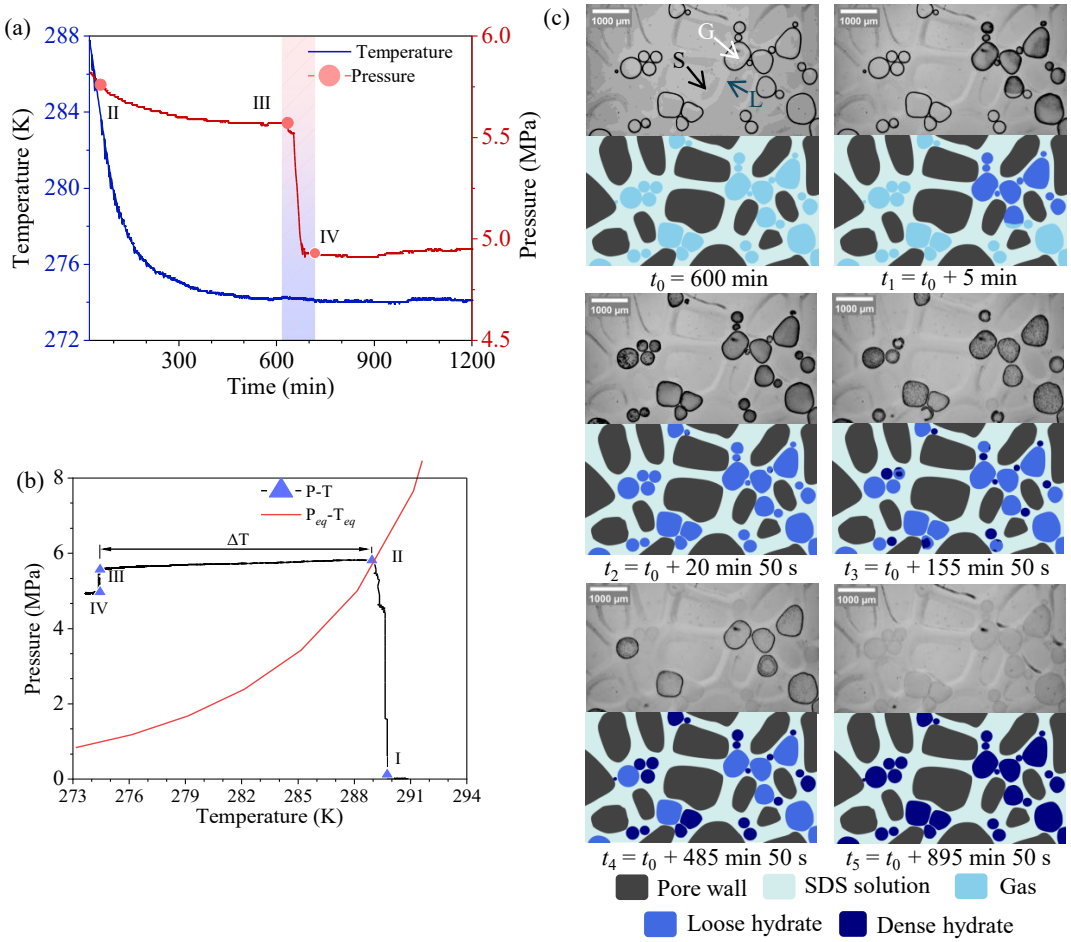


Fig. 2. Formation of bubble-derived hydrates: (a) Temperature and pressure evolution, (b) P-T trajectory and (c) Sequential micrographs of hydrate development.

was linearly ramped at a rate of 1 K/h until reaching ambient temperature (~ 298 K). Real-time changes in hydrate morphology, as well as the corresponding pressure and temperature variations, were continuously recorded until the system stabilized at a final state.

3. Results and discussion

3.1 Formation kinetics and morphological evolution at the pore scale

3.1.1 In-situ observation and thermodynamic trajectory of hydrate formation

To evaluate how the imposed cooling path affects hydrate nucleation and growth, the thermodynamic evolution during hydrate formation was monitored, with the corresponding pressure and temperature trajectory presented in Fig. 2(a). The system was cooled from room temperature to 274 K. At approximately 650 min, the pressure gradually decreased from ~ 5.5 to ~ 5.0 MPa, at an average rate of approximately 0.36 MPa/h, accompanied by a transient 0.4 K temperature rise. This thermal spike arose from the exothermic nature of hydrate formation, while the concurrent pressure decline resulted from continuous gas consumption. Rapid thermal equilibration followed immediately, owing to the high thermal conductivity of the glass microfluidic chip.

To determine whether the applied pressure-temperature path had entered the hydrate stability zone and triggered the formation of crystal nuclei, the experimental trajectory was compared with the calculated phase equilibrium curve. Fig. 2(b) presents the pressure-temperature (P-T) trajectory (black line) and the calculated hydrate phase equilibrium curve (red line). The process initiates at point I (~290 K, 0 MPa), which lies outside the hydrate stability zone where nucleation is thermodynamically unfeasible. Subsequent pressurization shifts the system to point II (~289 K, 5.8 MPa), where the system first intersects the equilibrium curve; yet, the interfacial energy barrier initially suppresses the phase transition. Upon further cooling to point III (~274 K, 5.5 MPa), the system achieves a subcooling of ~15 K, accompanied by a slight pressure reduction to ~5.5 MPa due to gas dissolution. A pronounced inflection appears between points III and IV; gradual pressure declines from 5.5 to 5.0 MPa, indicating that the nucleation energy barrier has been overcome and massive hydrate formation has ensued. The trajectory terminates at point IV (~274 K, 5.0 MPa), establishing a stable P-T equi-

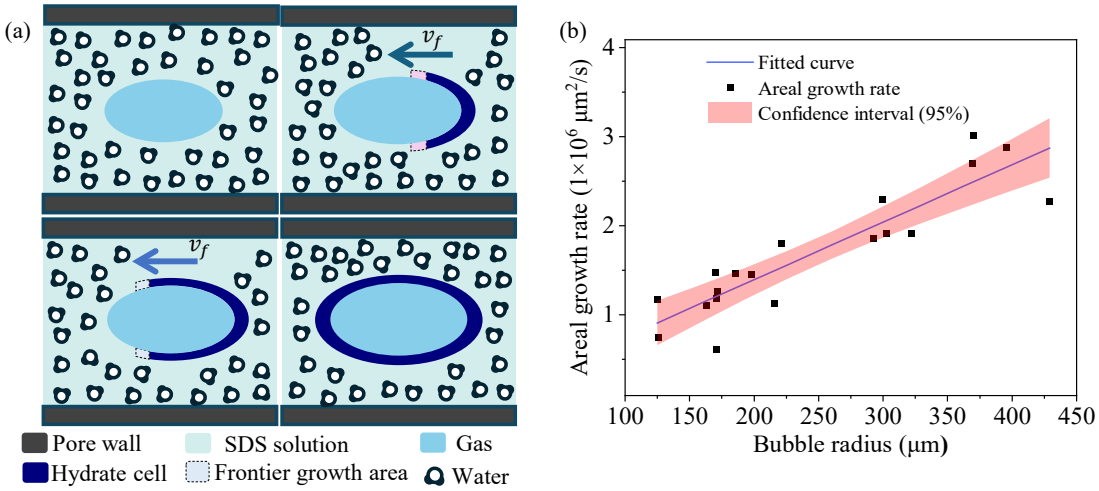


Fig. 3. Effect of bubble size on hydrate film growth kinetics: (a) Growth-front schematic and (b) areal growth rate versus equivalent bubble radius.

librium. The operating state remains consistently above the equilibrium curve, confirming that sustained hydrate growth is driven by the imposed subcooling process.

To assess how the initial bubble size influences the subsequent phase transition, the size distribution of the initial bubbles and their morphological evolution were examined. Fig. S2 presents the size of initial gas bubbles and Fig. 2(c) shows the pore-scale microscopic phase transition in which transparent bubbles first convert into porous hydrate shells and then densify into dense hydrate particles. Upon subcooling, a semi-transparent, low-density hydrate shell appears instantaneously on the bubble surface (t_0-t_2), accompanied by a prominent reduction in optical transmittance. Then, water molecules diffuse through the porous shell and react with the encapsulated gas (t_3-t_5) until the entire bubble is fully converted into a compact hydrate grain (Fig. 2(c)).

Distinct reflectivity differences allow the unambiguous identification of coexisting phases within the pore space. The gas phase is the brightest (white arrow in Fig. 2(c)). The hydrophilic pore walls (black arrow) show a gray level similar to that of the aqueous solution, and the liquid domain is delineated by the gas-liquid interface (blue arrow). These observations align well with the phase-contrast criteria documented by Zhang et al. (2023).

3.1.2 Size-dependent growth kinetics of the porous hydrate shell

This section examines the transformation of gas bubbles into porous hydrate shells. To quantify the microscale kinetics, the 2D projected area of hydrates was monitored. Although hydrate growth is intrinsically three-dimensional, the geometric confinement of microfluidic channels restricts vertical expansion, allowing the particles to be approximated as quasi-2D objects. While this 2D analytical approach cannot capture minor vertical densification, it is a reliable and widely adopted method for quantifying hydrate growth (Ouyang et al., 2023). Because the bubbles were confined by pore throats and walls, their projected shapes were not perfectly circular. Therefore, the equivalent circular radius derived from the projected area does not represent the exact three-dimensional radius of an individual bubble; nevertheless, under the quasi-2D confinement of the microfluidic chip, it provides a consistent and reproducible descriptor of the in-plane bubble size. The resulting geometric uncertainty was controlled by applying the same projected-area-based metric to all particles and by interpreting the spherical-bubble scaling relationship only semi-quantitatively. As illustrated in Fig. S3, both the number of porous hydrate shells and their total projected area exhibit a clear stepwise growth trend. The hydrate count and total area increase most rapidly between t_1 and t_2, whereas the average area fluctuates substantially due to variations in initial bubble size. The growth rate then slows down markedly from t_2 to t_4 as the system stabilizes. Microscopic observations (Fig. S4) further confirm that bubbles preferentially accumulate at pore throats. In this chain reaction, hydrate formation on one bubble catalyzes crystallization in adjacent bubbles directly ("chain induction" effect). Furthermore, hydrate shell growth exhibits clear directionality, driven by pore-scale thermal gradients and cooling pathways.

To quantify the size-dependent growth kinetics, two characteristic parameters were defined: (i) The areal growth rate v_a, which describes the increment in the projected area of the hydrate shell per unit time, and (ii) the growth front velocity v_f, measured along the advancing three-phase boundary as marked by the arrows in Fig. 3(a). According to Fig. 3(b), there is a positive correlation between bubble area and the areal growth rate v_a. The areal growth rate v_a increases positively with the increase in the initial bubble area. The smallest bubble (Fig. S5(d)) has the smallest v_a, while larger bubbles show correspondingly higher values. However, due to the irregular shapes of some bubbles, the areal growth rate is affected (Figs. S5(b) and S5(c)). In contrast, tracking the radial advance of the hydrate growth front reveals that v_f remains nearly constant across the full range of investigated bubble sizes.

To explain the pore-scale mechanism that controls the propagation of hydrate films, this study conducted a schematic

analysis of the interface growth process. Fig. 3(a) illustrates the interfacial mechanism of hydrate film propagation. Under low-temperature and high-pressure conditions, the gas-liquid interface features a higher specific Gibbs free energy than the bulk liquid, making it the preferred site for gas hydrate nucleation. Hydrate crystals propagate along the three-phase contact line until the entire bubble surface is covered, and this gas-liquid-solid contact region is defined as the growth front zone. As the reaction proceeds, the hydrate film thickens preferentially toward the bulk liquid phase, leading to a gradual increase in shell volume. This growth behavior is consistent with the macroscopic observations by Li et al. (2014b), where hydrate film thickening and irregular growth were observed.

To rationalize these experimental findings, a kinetic model for hydrate film propagation was derived. The elementary reaction at the hydrate growth front is expressed as:

$$G + n_h H_2O \leftrightarrow G \cdot n_h H_2O \tag{1}$$

where G denotes a guest gas molecule and n_h is the hydration number. Since the Gibbs free energy change of the forward reaction is negative, the forward reaction is thermodynamically favorable and dominates the overall process. The bubble is surrounded by an excess of SDS aqueous solution, and the heat released by the exothermic reaction dissipates rapidly; thermal effects can therefore be neglected in the kinetic model. The kinetic formulation in Eqs. (1)-(8) follows the diffusion-kinetic model of Vlasov (2013, 2019), with symbols and equation numbering adapted to Table S1. The molar formation rate of the hydrate shell (r_h) is given by:

$$r_h = k'(c^* - c_e) \tag{2}$$

$$k' = k_i \left(\frac{\rho_w}{M_w}\right)^{n_h} \tag{3}$$

where k_i denotes the interfacial reaction rate constant, n_h denotes the dimensionless hydration number, ρ_w denotes the mass density of the aqueous phase, M_w denotes the molar mass of water, c^* denotes the molar concentration of dissolved gas adjacent to the growth front, c_e denotes the equilibrium dissolved-gas concentration at the growth front, and k' denotes the apparent rate constant dependent on the gas composition and temperature. A molar balance for hydrate at the growth front yields:

$$r_h = \frac{\rho_h}{M_h} v_f \tag{4}$$

Combining Eqs. (2) and (4) yields the expression for the growth front velocity v_f:

$$v_f = \frac{M_h k'(c^* - c_e)}{\rho_h} \tag{5}$$

where ρ_h and M_h are the density and molar mass of the hydrate, respectively.

The model further defines $\mathbf{J}$ as the molar flux vector of the dissolved gas, β as the mass-transfer coefficient, c_s as the dissolved-gas concentration at the gas-liquid interface, c^* as the dissolved-gas concentration at the growth front; and c_e as the equilibrium dissolved-gas concentration at the growth front. Assuming that all gas molecules diffusing to the growth front are consumed by hydrate formation, the molar flux of gas equals its molar consumption rate:

$$\mathbf{J} = \beta(c_s - c^*) = |r_g| \tag{6}$$

$$r_h = -r_g \tag{7}$$

where r_h and r_g are the molar rates of hydrate formation and gas consumption per unit interfacial area, respectively (negative values indicate reactant depletion).

Combining Eqs. (2), (6) and (7) yields the gas concentration at the growth front:

$$c^* = \frac{k' c_e + \beta c_s}{k' + \beta} \tag{8}$$

By substituting Eq. (8) into Eq. (5) and introducing the growth-front combined rate constant k^*, the growth front velocity v_f can be rewritten as:

$$v_f = \frac{M_h k^* \Delta c}{\rho_h} \tag{9}$$

$$\frac{1}{k^*} = \frac{1}{k'} + \frac{1}{\beta} \tag{10}$$

where Δc is the overall concentration driving force. Eq. (9) indicates that v_f depends only on Δc and k^*, independent of bubble size. Here, $\Delta c = c_s - c_e$.

From a geometric perspective, the areal growth rate v_a is the product of the front velocity v_f and the perimeter of the growth front C_p:

$$v_a = v_f C_p \tag{11}$$

For an ideal spherical bubble, C_p is proportional to the equivalent circular radius R_e:

$$C_p \propto R_e \tag{12}$$

Combining Eqs. (11) and (12) indicates that v_a increases linearly with R_e, which aligns well with the experimental data shown in Fig. 3(b). Notably, this idealized relationship assumes a regular bubble geometry, as irregular morphologies induced by strong pore confinement may cause local deviations in C_p. Accordingly, this formulation serves as a semi-quantitative interpretation of the observed size-dependent kinetics, rather than a rigorous analytical solution. Nevertheless, it provides a consistent physical basis for the core observation that v_f is independent of bubble size while v_a increases with bubble dimensions.

The contrasting scaling of growth-front velocity and areal growth rate provides a useful diagnostic for separating local interfacial kinetics from the geometric amplification caused by bubble size. At a fixed concentration driving force, the front velocity is controlled by the combined reaction and mass-transfer resistance at the advancing interface, so it remains nearly independent of bubble size. The areal growth rate, however, is the product of this velocity and the perimeter of the growth front, which increases with the equivalent radius. This distinction explains why larger bubbles can consume more hydrate-forming material per unit time even when the local front advances at a similar rate. In the confined pore network, neighboring bubbles may also alter local gas availability

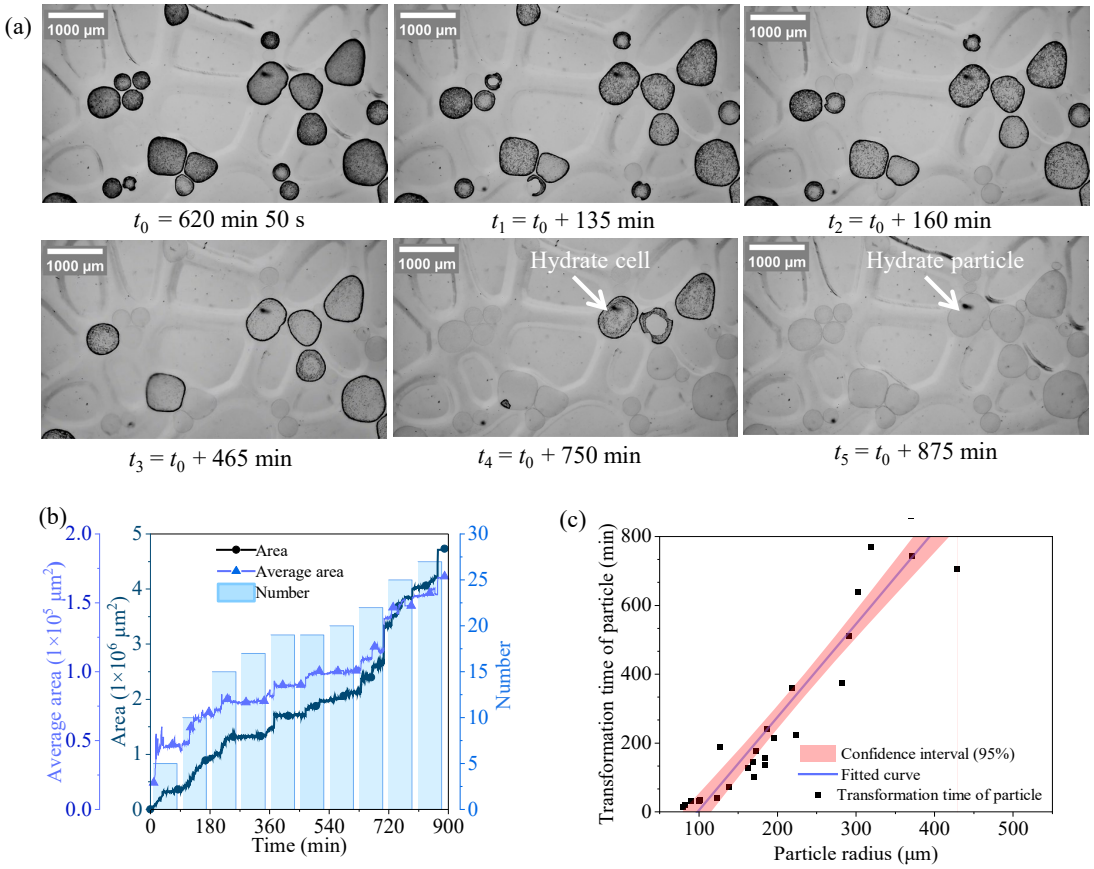


Fig. 4. Densification of bubble-derived hydrate particles: (a) Time-lapse micrographs, (b) particle number and projected-area evolution and (c) densification time versus particle radius.

and interfacial curvature, providing a plausible route for the observed chain-induction behavior. The scaling relation should nevertheless be interpreted as a semi-quantitative envelope for the tested morphologies, because irregular shells, contact with pore walls, and local variations in film thickness can all perturb the idealized perimeter-based estimate.

3.1.3 Two-stage densification behavior and quantitative kinetic model

High-resolution *in-situ* visualization captures the full morphological transition from porous hydrate shells to dense hydrate grains, which proceeds via two distinct stages, as illustrated in Fig. 4(a). In the initial rapid densification stage (t_0-t_2), the as-formed porous shell develops pronounced surface roughness and gradually becomes optically transparent. Small particles with projected areas of $2\times10^3\sim1\times10^4$ μm^2 complete conversion first because of their limited internal gas volume. Their thin, highly permeable shells impose negligible mass-transfer resistance, resulting in a maximum densification rate. During the subsequent slow densification stage (t_3-t_5), the remaining larger particles with projected areas of $3\times10^4\sim6\times10^4$ μm^2 continue to increase in brightness as trapped internal gas is progressively consumed. Residual gas pockets (marked by white arrows in the fourth frame of Fig. 4(a)) shrink continuously until the entire particle is converted into a compact, dense hydrate grain (white arrows in the fifth frame of Fig. 4(a)). This two-stage densification behavior is further confirmed by the temporal evolution of particle number, total converted area, and average projected area, as plotted in Fig. 4(b).

The total densification time exhibits a clear particle size dependence, as summarized in Fig. 4(c). Constrained by the pore network geometry, approximately 75% of the bubbles have radius ranging from 50 to 200 μm and achieve full densification within 400 min. The larger particles with radius of (200 ~ 450) μm require substantially longer times, ranging from 400 to 900 min. This prolonged duration arises from two coupled factors: The larger volume of trapped gas that must be converted, and the progressively thickening hydrate shell that imposes increasing diffusional resistance to mass transport across the solid phase.

During this stage, hydrate formation proceeds simultaneously on both the outer and inner surfaces of the porous shell via two parallel pathways: (1) On the outer surface, dissolved gas from the bulk liquid accumulates at the crystal interface, driving outward thickening of the shell; (2) On the inner surface, trapped gas diffuses outward through the porous hydrate matrix and reacts with water molecules that have diffused inward from the bulk phase. Given that gas concentration inside the shell is far higher than that in

the surrounding liquid, the coupled inward water diffusion and outward gas transport through the shell dominates the overall conversion process and governs the final densification yield. Accordingly, the overall reaction rate is fundamentally controlled by mass transfer through the hydrate shell. The coexistence of outer-surface and inner-surface conversion also implies that densification cannot be represented by a single moving reaction front. Outward growth is mainly controlled by the supply of dissolved gas and water through the surrounding liquid, whereas inward conversion depends on the internal gas reservoir and the permeability of the hydrate framework. As the shell becomes denser, these two pathways become increasingly asymmetric: the outer interface can remain chemically active, but the inward transport of reactants and the outward release of products are progressively restricted. This asymmetry helps explain why particles with similar external dimensions can exhibit different conversion times when their internal pore structures or contact geometries differ. It also suggests that treatments designed to alter shell permeability may be more effective than temperature changes alone after the initial densification phase. In the present micromodel, the observed brightness increase, indentation, and eventual grain formation provide qualitative evidence for this coupling, even though the local permeability field could not be measured directly.

To quantitatively describe this radial densification process, the classical kinetic framework of Englezos et al. (1987) was adopted, which describes hydrate growth as an interfacial crystallization process driven by fugacity difference. It has been widely validated for isothermal radial growth of spherical hydrate particles (Li et al., 2014a; Yin et al., 2018; Yan et al., 2025). In this model, the molar formation rate of hydrate for a single particle is expressed as:

$$\frac{\mathrm{d}n_p}{\mathrm{d}t} = K_1^* A_p (f - f_e) \tag{13}$$

$$\frac{1}{K_1^*} = \frac{1}{k_r} + \frac{1}{k_d} \tag{14}$$

Eq. (13) is adapted from Englezos et al. (1987), with the notation $K_1{}^*$ and A_p, where $K_1{}^*$ represents the overall kinetic rate constant integrating the interfacial reaction rate constant k_r and the cross-shell mass-transfer rate constant k_d. A_p denotes the outer surface area of the hydrate particle, and $(f - f_e)$ is the fugacity difference acting as the thermodynamic driving force for hydrate growth. Here, n_p is the molar amount of hydrate in an individual particle, f is the fugacity of dissolved gas, and f_e is its equilibrium fugacity.

The temperature dependence of k_r is described by the Arrhenius relationship (Laidler, 1984):

$$k_r = k_0 \exp\left(-\frac{\Delta E_a}{RT}\right) \tag{15}$$

where k_0 denotes the pre-exponential factor of the interfacial reaction rate constant, ΔE_a denotes the activation energy, R denotes the universal gas constant, and T is the local temperature.

Under the uniform temperature and pressure conditions maintained in the micromodel, $K_1{}^*$ and $(f - f_e)$ remain constant across all particles. Therefore, Eq. (13) indicates that the hydrate formation rate $\mathrm{d}n_p/\mathrm{d}t$ of an individual particle increases linearly with the surface area A_p, which provides a direct physical explanation for the size-dependent densification time observed in Fig. 4(c). For an approximately spherical particle where $V_p \propto {R_e}^3$ and $A_p \propto {R_e}^2$, the total moles of hydrate produced equals the formation rate multiplied by the densification time. Combining these relationships yields the total densification time as:

$$V_p = C_1 R_e^3,\ A_p = C_2 R_e^2 \tag{16}$$

$$\frac{\mathrm{d}n_p}{\mathrm{d}t} t_d = \frac{V_p \rho_h}{M_h} \tag{17}$$

where C_1 and C_2 represent geometric shape factors, and t_d is the total densification time. Here, V_p is the particle volume.

Combining Eqs. (13), (16) and (17) yields the total densification time t_d:

$$t_d = \frac{C_1 R_e^3 \rho_h}{K_1^* C_2 R_e^2 (f - f_e) M_h} \tag{18}$$

Simplifying the geometric terms (for ideal spheres, $C_1/C_2 = 1/3$) gives the final relationship:

$$t_d = \frac{1}{3} \frac{\rho_h R_e}{K_1^* (f - f_e) M_h} \tag{19}$$

Eq. (19) demonstrates that the total densification time t_d increases linearly with the equivalent particle radius R_e and is inversely proportional to both the overall kinetic rate constant $K_1{}^*$ and the fugacity driving force $(f - f_e)$. This theoretical prediction is in line with the experimental data shown in Fig. 4(c), which confirms the size dependence of the densification time. The densification expression also clarifies which assumptions control the predicted linear dependence of conversion time on particle radius. The model treats the particle as approximately spherical and represents the volume and surface area with constant geometric shape factors. These simplifications are appropriate for isolating the first-order effect of size, but they do not fully account for ellipsoidal particles, contact with pore walls, or spatial variations in shell permeability. As the shell thickens, a small change in its effective diffusion resistance can produce a disproportionately large change in the conversion time, especially for particles that retain a large internal gas reservoir. The agreement with the measured trend therefore supports the dominant role of size-dependent mass-transfer resistance, while the residual scatter reflects real differences in morphology and local pore geometry. The resulting scaling should be used to compare kinetic regimes rather than as an exact prediction for every individual particle.

The micro-morphological and optical evolution during densification is further illustrated in Fig. S6. The time-lapse sequence in Fig. S6(a) (t_0-t_9) records the complete transformation of a bubble-encapsulating hydrate shell into a dense grain, consistent with *in-situ* Raman observations reported by Zhang et al. (2026), who detected both the methane gas peak at 2,917.2 cm^{-1} and the structure I hydrate large-cage signature at 2,907.6 cm^{-1}. As densification proceeds, continuous gas consumption reduces the internal pressure inside the shell. The

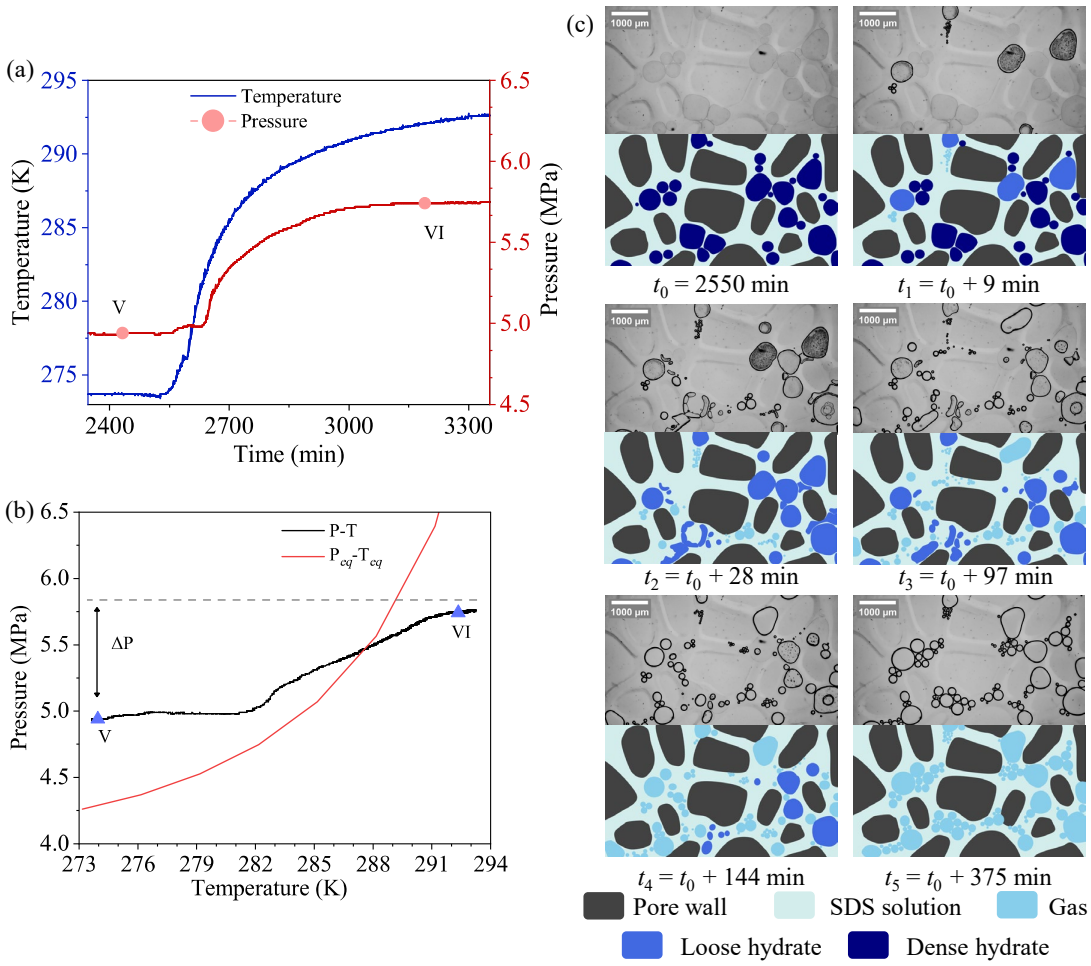


Fig. 5. Heating-induced hydrate dissociation: (a) Temperature and pressure evolution, (b) P-T trajectory versus equilibrium curve and (c) time-lapse micrographs of two-stage dissociation.

higher external confining pressure then compresses the flexible hydrate shell inward, forming distinct concave indentations on the particle surface. This observation is consistent with the hydrate shell deformation phenomenon reported by Sun et al. (2019) during hydrate formation on millimeter-scale bubbles.

To quantify the optical contrast accompanying hydrate shell densification, pixel intensity profiles were measured along the central dashed lines of two representative particles (particle 1 and particle 2 in Fig. S6(a)) using ImageJ. Fig. S6(b) tracks the pixel intensity profiles (0-255 gray scale). During t_1-t_3, the fluctuating gray values in the core region (pixels 100-400) reflect the structural rearrangement and initial collapse of the porous hydrate shell. From t_4 to t_9, the gray values increase steadily from ~140 to ~200, indicating the progressive optical clarification of particle center as the shell densifies, which matches the visual trend in Fig. S6(a).

Constrained by the pore walls, hydrate particles predominantly exhibit an ellipsoidal morphology, being narrower in the longitudinal direction and flatter in the transverse direction. During the inward growth of the hydrate shell, the transformation process displays distinct spatial anisotropy: The conversion completes preferentially in the longitudinal direction (the second schematic panel of Fig. S6(c)) before advancing transversely (the third schematic panel of Fig. S6(c)). Throughout both stages, the particles exhibit a characteristic "bright core, dark edge" optical contrast (yellow dashed boxes in the seventh and ninth frames of Fig. S6(a)). The final dense grain (the fourth schematic panel of Fig. S6(c)) is achieved when all trapped natural gas is fully converted into solid hydrate. This optical contrast originates from the difference in physical structure, as illustrated in Fig. S6(d). The porous hydrate shell is a gas-solid mixture with abundant internal interfaces that cause strong light scattering and refraction, resulting in a dark, opaque appearance. On the other hand, fully dense hydrate grains are homogeneous single-phase solids with a uniform refractive index, which minimizes light attenuation and yields a highly transparent morphology.

3.2 Two-stage dissociation of gas hydrate grains

3.2.1 Pore-scale visualization and thermodynamic characteristics of dissociation

Hydrate dissociation is initiated via controlled heating under constant-volume conditions. As illustrated in Fig. 5(a), the chip temperature rises from 274 to 292 K (corresponding

to the transition from stage V to stage VI), and the system internal pressure increases abruptly from ~ 5.0 to ~ 5.7 MPa. This sharp pressure uplift directly reflects the rapid release of gas from hydrate dissociation. Fig. 5(b) plots the experimental pressure-temperature (P-T) trajectory (black line) against the calculated hydrate phase equilibrium curve (red line). When the system state lies above the equilibrium curve (high-pressure, low-temperature region), hydrate remains thermodynamically stable. As heating proceeds, the P-T trajectory crosses the equilibrium curve and enters the unstable region, upon which sustained hydrate dissociation commences.

Quantitative tracking of the projected bubble area reveals two distinct kinetic regimes during the dissociation process (Fig. S7). First, during the initial rapid dissociation stage (t_0-t_2, ~50 min), internal hydrate breakdown generates a heterogeneous gas-liquid-solid mixture that appears dark under optical observation. This highly efficient stage accounts for about 80% of the total volume conversion. Second, in the subsequent slow stage (t_3-t_5, ~ 300 min), the outer dense hydrate shell gradually breaks apart, releasing small gas bubbles. The color-coded image sequence in Fig. 5(c) further visualizes the stepwise evolution of each phase, providing direct pore-scale evidence for the two-stage dissociation behavior. The time scales reported in Figs. S7, S8 and S9 refer to different levels of analysis. Fig. S7 illustrates the ensemble-averaged evolution of all particles within the camera field of view, whereas Figs. S8 and S9 present the time-lapse evolution of one representative particle. Therefore, the approximately 50-min rapid stage and the approximately 300-min slow stage obtained from Fig. S7 are not expected to be identical to the 69-min Stage I and 216-min Stage II observed for the representative particle.

3.2.2 Two-stage dissociation behavior and rate-limiting mechanisms

In-situ microscopic observations reveal that dense hydrate particles, composed of a structurally stable outer shell and an inner hydrate core, follow a two-stage dissociation pathway: Preferential internal dissociation and then delayed shell breakdown, as visualized in Figs. S8 and S9.

Stage I (t_0-t_9) is dominated by internal dissociation. From t_0 to t_3, the outer shell in direct contact with the bulk liquid dissociates first, generating porous channels that allow the escape of internal dissociated products. As heating continues (t_4-t_7), the outer shell retains its structural integrity. Meanwhile, the internal hydrate dissociates rapidly and continuously, which generates numerous dispersed microbubbles (outlined by white dashed lines in Fig. S8) that gradually coalesce and expand. By t_8, a large gas bubble is fully formed and trapped within the remaining intact hydrate shell. In the subsequent approximately 60 min period (t_8-t_9), the dissociation reaction mainly continues to expand outward along the contact surface between the internal gas bubble and the hydrate shell, and this process accounts for the majority of the time in the first stage. It should be noted that Fig. S8 shows the dissociation stage of a single hydrate particle, while Fig. S7 presents the overall evolution of all particles in the field of view. Although the first stage period of the dissociation of each bubble varies due to differences in the initial particle size and the start time of dissociation, the overall dissociation cycle is basically consistent with the macroscopic evolution time scale shown in Fig. S7.

Stage II (t_9-t_{17}) is dominated by outer hydrate shell dissociation. By t_9, the inner hydrate core has been completely converted into gas and water, leaving only the dense outer shell. During t_{10}-t_{13}, the shell begins to fracture and form localized breaches (marked by red dashed lines in Fig. S9). The pressure difference across the shell drives the trapped gas to escape through these openings, causing local surface depressions on the particle due to rapid pressure release. In the final stage (t_{14}-t_{17}), the remaining loose hydrate shell (blue boxes in Fig. S9) progressively dissociates and the released gas bubbles continue to coalesce until full dissociation is achieved.

The overall dissociation mechanism is schematically summarized in Fig. 6. Clearly, hydrate dissociation is a complex multiphase process governed by intrinsic reaction kinetics, heat transfer and mass transfer. The experimental results demonstrate that the process is controlled by coupled heat and mass transfer, with a clear regime transition: Heat transfer dominates Stage I, whereas mass transfer becomes the rate-limiting factor in Stage II.

During the rapid dissociation Stage I, convective heat transfers from the bulk liquid to the hydrate particle surface. Thermal energy is absorbed to overcome the crystal lattice binding energy and trigger phase dissociation. The delayed dissociation of the outer hydrate shell indicates a higher degree of structural integrity, whereas the preferential dissociation of the internal core may be attributed to a higher density of intrinsic crystal microdefects, although these defects are not directly resolved in the present images. Thermodynamically, these structural imperfections may locally reduce the activation energy for dissociation, thus acting as favorable initiation sites for phase transition. Furthermore, rising temperatures and pressure changes also cause pre-dissolved gas to form microbubbles, which further accelerates this internal dissociation. This stage, which is consistent with a possible defect-assisted mechanism, is characterized by an irregular dissociation front and a high apparent dissociation rate. Following the classical Kim-Bishnoi model (Kim et al., 1987), the endothermic dissociation rate depends on three key factors: The fugacity driving force ($f - f_e$), the hydrate-fluid interfacial area (A_p) and the kinetic rate constant (k_h). This mass-transfer resistance causes gas to accumulate inside the particle, elevating the local internal pressure and reducing the thermodynamic driving force for further dissociation. The observations also indicate a size effect on dissociation initiation: Larger grains generally initiate dissociation earlier (e.g., the preferential dissociation of large particles at t_1 in Fig. 5(c)). This trend may be related to their larger heat-absorbing surface area, although the internal temperature field was not measured directly.

During the slow dissociation Stage II, mass transfer gradually replaces heat transfer as the dominant rate-limiting factor. Physically, the intact dense outer shell acts as a low-permeability barrier that blocks the outward transport of natural gas. Consequently, the overall dissociation rate is predominantly limited by the diffusion of released gas through the solid hydrate shell. To semi-quantitatively describe this

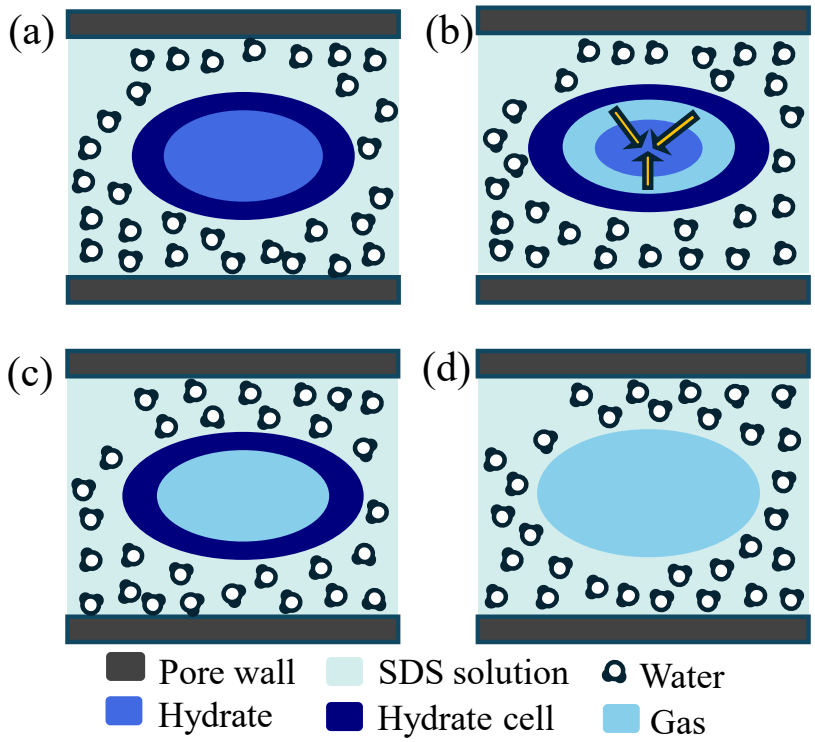


Fig. 6. Two-stage mechanism of hydrate dissociation. (a) Inner-layer dissociation; (b) dissociation-front propagation; (c) outer-shell dissociation; (d) complete dissociation.

diffusion-limited process, the mass transport is formulated by Fick's first law (Fick, 1855):

$$\mathbf{J} = -D_e \frac{\mathrm{d}c}{\mathrm{d}x} \tag{20}$$

where $\mathbf{J}$ denotes the molar flux of gas (the amount of gas passing through unit area per unit time), D_e represents the effective diffusion coefficient of the gas within the hydrate shell, c is the dissolved-gas concentration, x is the diffusion path length, and $\mathrm{d}c/\mathrm{d}x$ represents the concentration gradient along the diffusion direction.

Eq. (20) indicates that gas diffuses from regions of high to low concentration, with the diffusion rate positively correlated with both the concentration gradient and the effective diffusion coefficient D_e. In Stage II, the dense outer shell acts as a physical barrier with a very low D_e, blocking the escape of internal gas. This mass-transfer resistance would cause gas to accumulate inside the particle, elevating the local internal pressure and reducing the thermodynamic driving force for further dissociation, consistent with the observed slowdown of Stage II.

Quantitatively, the experimental data show a pronounced kinetic contrast between two stages. The rapid Stage I (t_0-t_9 in Figs. S8 and S9) finishes within 69 min, and further evidence of this is provided during the hydrate shell dissociation period (t_8-t_9), where the remaining hydrate shell layer is identified as the main obstacle determining the overall dissociation rate. The slow dissociation Stage II (t_9-t_{17} in Fig. S9) lasts for approximately 216 min. The observed slow dissociation stage suggests that increasing the heating input alone may not proportionally enhance gas release once a dense hydrate shell has formed. Thermal-stimulation strategies should therefore consider both heat delivery and the mass-transfer resistance of the hydrate shell. These results have practical implications for the design of thermal stimulation strategies. Increasing the heating rate may effectively accelerate the early internal dissociation, but the benefit can diminish once a dense outer shell controls gas release. A staged strategy that first supplies sufficient heat to initiate internal conversion and then maintains favorable pressure conditions for gas transport may therefore use energy more efficiently than a uniformly high heating rate. The size distribution of trapped bubbles should also be considered, because larger particles store more gas but require longer conversion and may form more effective transport barriers. The practical implication is that bubble-size distribution should be treated as an operating variable rather than a fixed geological property. During the early stage of thermal stimulation, a population dominated by large bubbles provides a larger interfacial area and a greater internal gas inventory, which can sustain rapid initial dissociation. As densification and shell formation proceed, however, these same particles may become persistent mass-transfer barriers that prolong the slow stage and reduce the benefit of additional heating. Production schemes may therefore benefit from staged heating: supplying sufficient heat at the beginning to promote dissociation, then controlling the temperature and pressure history so that gas can escape before the outer shell becomes fully consolidated. In field settings, local bubble size will also depend on gas seepage rate, pore-throat geometry, salinity, and

the rate of temperature change. The present experiments isolate the size effect under controlled conditions, but the observed transition from interface-controlled to transport-controlled behavior provides a physically consistent basis for coupling bubble-size distributions with heat delivery and permeability evolution in reservoir-scale models. The present pore-scale observations provide a basis for incorporating bubble size, shell permeability, and the heat-to-mass-transfer transition into reduced-order models of hydrate dissociation. Such models would be more representative of heterogeneous sediments than formulations based only on bulk temperature or pressure, although additional measurements under varying salinity, gas composition, and pore-network geometry are still needed.

4. Conclusions

This study quantitatively establishes the pore-scale kinetic dependence of gas hydrate phase transitions on discrete bubble sizes. The main quantitative findings and engineering implications are summarized as follows:

1) Gas hydrate formation around gas bubbles proceeds via a well-defined two-stage pathway, consisting of rapid hydrate shell formation followed by gradual densification. During the initial shell propagation stage, the growth front velocity remains independent of bubble size, as it is governed solely by the interfacial concentration driving force and the intrinsic kinetic rate constant. In contrast, the areal growth rate scales linearly with the equivalent bubble radius, accompanied by a distinct "chain induction" effect between adjacent bubbles that accelerates overall crystallization. During the subsequent densification stage, the total time required for full conversion into dense hydrate grains increases linearly with the equivalent bubble radius. This size dependence arises from the progressively enhanced mass-transfer resistance across the thickening hydrate shell, which dominates the overall conversion kinetics.
2) The thermal dissociation of dense hydrate grains follows a two-stage pathway, transitioning from a fast stage that is consistent with defect-assisted internal dissociation to a mass-transfer-limited slow stage. In the fast stage, pre-existing microdefects and entrapped microbubbles inside the grains may act as preferential initiation sites and likely drive the rapid internal dissociation that accounts for over 80% of the total hydrate conversion within approximately 50 min. The endothermic internal dissociation may exert a thermal-shielding effect on the dense outer shell and also appears to delay its structural breakdown. In the subsequent slow stage, the intact outer hydrate shell acts as a low-permeability barrier that hinders outward gas diffusion. The resulting gas accumulation may increase the local internal pressure and reduce the effective thermodynamic driving force, thereby contributing to the observed decrease in the overall dissociation rate. Bubble size also affects the onset of dissociation, with larger grains generally initiating dissociation earlier due to their larger heat-absorbing surface area.

These results demonstrate that discrete bubble size influences both the formation and dissociation kinetics of gas hydrates through changes in interfacial growth area, internal gas volume, and hydrate-shell mass-transfer resistance. These findings provide a pore-scale basis for incorporating bubble-size distributions and shell-controlled gas transport into models of thermal stimulation and gas production. Within the tested bubble-size range and thermal-stimulation conditions, the findings provide mechanistic guidance for evaluating the heating rate, temperature window, and pressure-maintenance strategies in hydrate production.

Acknowledgments

This work was supported by the National Natural Science Foundation of China (Nos. 42576237 and 52206268), the Shenzhen Science and Technology Program (No. JCYJ20250604144911016), and the Natural Science Foundation of Top Talent of SZTU (No. GDRC202314).

Supplementary file

https://doi.org/10.46690/ager.2026.09.07

Conflicts of interest

The authors declare no competing interest.

Open Access This article is distributed under the terms and conditions of the Creative Commons Attribution (CC BY-NC-ND) license, which permits unrestricted use, distribution, and reproduction in any medium, provided the original work is properly cited.

References

Almenningen, S., Lysyy, M., Ersland, G. Quantification of CH_4 hydrate film growth rates in micromodel pores. Crystal Growth & Design, 2021, 21(7): 4090-4099.

Ballard, L., Sloan, E. D. The next generation of hydrate prediction IV: A comparison of available hydrate prediction programs. Fluid Phase Equilibria, 2004, 216(2): 257-270.

Cui, Y., Lu, C., Wu, M., et al. Review of exploration and production technology of natural gas hydrate. Advances in Geo-Energy Research, 2018, 2(1): 53-62.

Englezos, P., Kalogerakis, N., Dholabhai, P. D., et al. Kinetics of formation of methane and ethane gas hydrates. Chemical Engineering Science, 1987, 42(11): 2647-2658.

Fang, B., Zhang, Z., Zhang, Q., et al. Molecular insights into two-phase flow in clay nanopores during gas hydrate recovery: Wettability-induced multiple pathways of water lock formation. Advances in Geo-Energy Research, 2025, 17(1): 17-29.

Fick, A. Ueber diffusion. Annalen der Physik, 1855, 170(1): 59-86.

Gong, B., Lei, G., Chen, L., et al. Mitigating risks in deep sea gas hydrate production: A new perspective on interpreting thermo-hydro-mechanical feedbacks. Advances in Geo-Energy Research, 2025, 17(3): 267-270.

Islam, M. R. A new recovery technique for gas production from Alaskan gas hydrates. Journal of Petroleum Science and Engineering, 1994, 11(4): 267-281.

Jang, J., Santamarina, J. C. Hydrate bearing clayey sediments: Formation and gas production concepts. Marine and

Petroleum Geology, 2016, 77: 235-246.

Ji, Y., Hou, J., Zhao, E., et al. Pore-scale study on methane hydrate formation and dissociation in a heterogeneous micromodel. Journal of Natural Gas Science and Engineering, 2021, 95: 104230.

Kim, H. C., Bishnoi, P. R., Heidemann, R. A., et al. Kinetics of methane hydrate decomposition. Chemical Engineering Science, 1987, 42(7): 1645-1653.

Laidler, K. J. The development of the Arrhenius equation. Journal of Chemical Education, 1984, 61(6): 494.

Li, B., Li, X.-S., Li, G. Kinetic studies of methane hydrate formation in porous media based on experiments in a pilot-scale hydrate simulator and a new model. Chemical Engineering Science, 2014a, 105: 220-230.

Li, S., Zhang, N., Hu, Z., et al. Visual experimental study on hydrate occurrence patterns and growth habits in porous media. Chemical Engineering Science, 2022, 262: 117971.

Li, S. -L., Sun, C. -Y., Liu, B., et al. New observations and insights into the morphology and growth kinetics of hydrate films. Scientific Reports, 2014b, 4(1): 4129.

Li, X., Wang, C., Li, Q., et al. Study on the growth kinetics and morphology of methane hydrate film in a porous glass microfluidic device. Energies, 2021, 14(20): 6814.

Li, X., Wang, C., Li, Q., et al. Experimental observation of formation and dissociation of methane hydrate in a micromodel. Chemical Engineering Science, 2022, 248: 117227.

Li, X., Wang, C., Liang, S., et al. Experimental visualization of cyclopentane hydrate dissociation behavior in a microfluidic chip. Chemical Engineering Science, 2020, 227: 115937.

Li, X., Wang, Y., Li, X., et al. Pore-scale investigation on the morphology evolution and micro-mechanism of methane hydrate formed from free gas and dissolved gas. Chemical Engineering Science, 2024, 293: 120055.

Li, Y., Xie, Y., Zhang, K., et al. CO_2 hydrate microscopic phase transition behavior based on microfluidic chips. Energy, 2025, 338: 138944.

Liu, Q., Li, S., Jiang, L., et al. Behaviors of methane hydrate formation and growth with halo. Applied Energy, 2025, 381: 125131.

Liu, Q., Liu, Y., Xu, J., et al. A review of the gas hydrate phase transition with a microfluidic approach. Energy Reviews, 2023, 2(1): 100011.

Liu, Z., Shao, Z. -Z. The diversity of alkane degrading bacteria in the enrichments with deep sea sediment of the South China Sea. Acta Microbiologica Sinica, 2007, 47(5): 869-873.

Lu, Z., Wang, L., Guo, Z., et al. The microfluidic in geo-energy resources: Current advances and future perspectives. Advances in Geo-Energy Research, 2025, 16(2): 171-180.

Moridis, G. J., Collett, T. S., Dallimore, S. R., et al. Numerical studies of gas production from several CH_4 hydrate zones at the Mallik site, Mackenzie Delta, Canada. Journal of Petroleum Science and Engineering, 2004, 43(3): 219-238.

Muraoka, M., Yamamoto, Y., Tenma, N. Simultaneous measurement of water permeability and methane hydrate pore habit using a two-dimensional glass micromodel. Journal of Natural Gas Science and Engineering, 2020, 77: 103279.

Ouyang, Q., Komisar, D., Ilchenko, O., et al. Raman assisted microfluidic insights into CO_2 hydrate dynamics and subsurface sequestration in confined space. Chemical Engineering Journal, 2025, 513: 162897.

Ouyang, Q., Pandey, J. S., von Solms, N. Microfluidic insights: Methane hydrate dynamics in distinct wettable confined space. Chemical Engineering Journal, 2023, 474: 145567.

Pang, Q., Yang, M., Gong, G., et al. Production characteristics of water-saturated methane hydrates under different thermodynamic conditions. Energy & Fuels, 2024, 38(4): 3057-3065.

Panieri, G., Copley, J. T., Linse, K., et al. Deep-sea gas hydrate mounds and chemosynthetic fauna discovered at 3,640 m on the Molloy Ridge, Greenland Sea. Nature Communications, 2025, 16: 11287.

Pardhi, D. S., Panchal, R. R., Raval, V. H., et al. Microbial surfactants: A journey from fundamentals to recent advances. Frontiers in Microbiology, 2022, 13: 982603.

Sloan, E. D. Fundamental principles and applications of natural gas hydrates. Nature, 2003, 426(6964): 353-359.

Sun, B., Liu, Z., Wang, Z., et al. Experimental and modeling investigations into hydrate shell growth on suspended bubbles considering pore updating and surface collapse. Chemical Engineering Science, 2019, 207: 1-16.

Sun, W., Kong, D., Li, Z., et al. Experimental investigation into gas migration mechanism in submarine sandy sediments at pore-scale. Advances in Geo-Energy Research, 2025, 17(1): 30-42.

Tang, L., Li, G., Feng, Z., et al. Mathematic modeling on thermal recovery of natural gas hydrate. Natural Gas Industry, 2006, 26(10): 105-107.

Uddin, M., Wright, F., Dallimore, S., et al. Gas hydrate dissociations in Mallik hydrate-bearing zones A, B, and C by depressurization: Effect of salinity and hydration number in hydrate dissociation. Journal of Natural Gas Science and Engineering, 2014, 21: 40-63.

Vlasov, V. A. Formation and dissociation of gas hydrate in terms of chemical kinetics. Reaction Kinetics, Mechanisms and Catalysis, 2013, 110(1): 5-13.

Vlasov, V. A. Diffusion-kinetic model of gas hydrate film growth along the gas-water interface. Heat and Mass Transfer, 2019, 55(12): 3537-3545.

Wang, G., Chen, X., Wang, S., et al. Influence of fracture connectivity and shape on water seepage of low-rank coal based on CT 3D reconstruction. Journal of Natural Gas Science and Engineering, 2022, 102: 104584.

Wang, G., Chu, X., Yang, X. Numerical simulation of gas flow in artificial fracture coal by three-dimensional reconstruction based on computed tomography. Journal of Natural Gas Science and Engineering, 2016, 34: 823-831.

Wang, G., Qin, X., Han, D., et al. Study on seepage and deformation characteristics of coal microstructure by 3D reconstruction of CT images at high temperatures.

International Journal of Mining Science and Technology, 2021, 31(2): 175-185.

Wang, Y., Yang, J., Wang, P., et al. Impact of multiphasic pore-scale interactions on gas hydrate formation and dissociation characteristics and kinetics: A microfluidic study. Lab on a Chip, 2025, 25(15): 3741-3765.

Wang, Z., Wu, X., Wang, L., et al. Mechanism of methane migration in oceanic hydrate system: Insights from microfluidic investigations. Marine and Petroleum Geology, 2024, 162: 106743.

Xu, H., Qin, Y., Wu, F., et al. Numerical modeling of gas extraction from coal seam combined with a dual-porosity model: Finite difference solution and multi-factor analysis. Fuel, 2022, 313: 122687.

Xu, H., Qin, Y., Yang, D., et al. Quantification of gas transport behavior during coalbed methane extraction in a coal seam considering a dual-porosity/single-permeability model. Natural Resources Research, 2024, 33(1): 321-345.

Xu, R., Kou, X., Wu, T.-W., et al. Pore-scale experimental investigation of the fluid flow effects on methane hydrate formation. Energy, 2023, 271: 126967.

Yan, X., Liu, J., Komiya, A., et al. A review of the visualization analysis of the pore-scale formation and decomposition of CO_2 hydrates for carbon capture and storage. Energies, 2025, 18(23): 6344.

Yao, S., Li, Y., Wang, W., et al. Experimental investigation on the microscopic decomposition process of natural gas hydrate particles. Energy & Fuels, 2019, 33(6): 5208-5215.

Yin, Z., Khurana, M., Tan, H. K., et al. A review of gas hydrate growth kinetic models. Chemical Engineering Journal, 2018, 342: 9-29.

Yin, Z., Moridis, G., Tan, H. K., et al. Numerical modelling of methane hydrate dissociation in sandy porous media by depressurization with a parametric study. In: Offshore Technology Conference Asia. Kuala Lumpur, Malaysia, 2018: OTC-28369-MS.

Zhang, G., Rogers, R. E., French, W. T., et al. Investigation of microbial influences on seafloor gas-hydrate formations. Marine Chemistry, 2007, 103(3-4): 359-369.

Zhang, J., Song, Z., Zhou, K., et al. Pore-scale analysis of the permeability and effective thermal conductivity of hydrate-bearing sediments based on a high-pressure microfluidics approach. Energy & Fuels, 2024a, 38(22): 22192-22204.

Zhang, J., Song, Z., Zhou, K., et al. Unveiling pore-scale methane hydrates growth kinetics using a novel high-pressure microfluidics coupled with *in-situ* Raman spectroscopy. Chemical Engineering Science, 2026, 321: 122903.

Zhang, J., Sun, H., Ge, Y., et al. Spatial distribution and phase transition characteristics of methane hydrate in the water-excess and gas-excess deposits. Energy & Fuels, 2024b, 38(5): 4047-4056.

Zhang, J., Yin, Z., Khan, S. A., et al. Path-dependent morphology of CH_4 hydrates and their dissociation studied with high-pressure microfluidics. Lab on a Chip, 2024c, 24(6): 1602-1615.

Zhang, Q., Yao, H., Jian, Z., et al. Gas-water flow behavior during hydrate dissociation using a developed 2.5D microfluidic chip. Energy & Fuels, 2023, 37(16): 11996-12006.

Zhang, X., Lu, X., Li, P. A comprehensive review in natural gas hydrate recovery methods. SCIENTIA SINICA Physica, Mechanica & Astronomica, 2019, 49(3): 034604.

Zhang, Y., Ji, Y., Qi, M., et al. Integrated detection of micro-pore structures and macro-mechanical responses for hydrate-bearing sediments. Advances in Geo-Energy Research, 2025a, 17(3): 184-195.

Zhang, Y., Liu, L., Luo, L., et al. Permeability prediction in hydrate-bearing sediments via pore network modeling. Advances in Geo-Energy Research, 2025b, 16(2): 158-170.

Zhong, J., Luo, Z., Zhu, Y., et al. Microfluidic investigation on CO_2 self-storage behavior in submarine sediment using artificial intelligence image recognition. Energy, 2025, 337: 138587.

Zhou, Z., Feng, J., Zeng, X., et al. Revealing the kinetic behaviors of hydrate formation on bubble surface with different pressure gradients in deep-sea methane seepage areas of the South China Sea. Energy, 2024, 308: 132808.